Structure of the $N = 27$ isotones derived from the ^{44}Ar$(d, p)^{45}$Ar reaction

L. Gaudefroy,[1,2] O. Sorlin,[1,3] F. Nowacki,[4] D. Beaumel,[1] Y. Blumenfeld,[1] Z. Dombrádi,[5] S. Fortier,[1] S. Franchoo,[1] S. Grévy,[3] F. Hammache,[1] K. W. Kemper,[6] K. L. Kratz,[7,8] M. G. St. Laurent,[3] S. M. Lukyanov,[9] L. Nalpas,[10] A. N. Ostrowski,[11] Yu.-E. Penionzhkevich,[9] E. C. Pollacco,[10] P. Roussel,[1] P. Roussel-Chomaz,[3] D. Sohler,[5] M. Stanoiu,[1] and E. Tryggestad[1]

[1]*IPN, IN2P3-CNRS, F-91406 Orsay Cedex, France*
[2]*CEA/DAM/DIF/DPTA/SPN Bruyères-le-Châtel, F-91297 ARPAJON Cedex, France*
[3]*Grand Accérateur National d'Ions Lourds (GANIL), CEA/DSM-CNRS-IN2P3, Bd Henri Becquerel, BP 55027, F-14076 Caen Cedex 5, France*
[4]*IReS, Univ. Louis Pasteur, BP 28, F-67037 Strasbourg Cedex, France*
[5]*Institute of Nuclear Research, H-4001 Debrecen, Pf. 51, Hungary*
[6]*Department of Physics, Florida State University, Tallahassee, Florida 32306, USA*
[7]*Max-Planck-Institut für Chemie, Otto-Hahn-Institut, D-55128 Mainz, Germany*
[8]*HGF Virtuelles Institut für Struktur der Kerne und Nukleare Astrophysik (VISTARS), D-55128 Mainz, Germany*
[9]*FLNR/JINR, 141980 Dubna, Moscow region, Russia*
[10]*CEA-Saclay, DAPNIA-SPhN, F-91191 Gif sur Yvette Cedex, France*
[11]*Institut für Kernchemie, Universität Mainz, D-55128 Mainz, Germany*

(Received 23 May 2008; published 11 September 2008)

The ^{44}Ar$(d, p)^{45}$Ar neutron transfer reaction was performed at 10A MeV. Measured excitation energies, deduced angular momenta, and spectroscopic factors of the states populated in ^{45}Ar are reported. A satisfactory description of these properties is achieved in the shell model framework using a new $sdpf$ interaction. The model analysis is extended to more exotic even-Z nuclei down to $^{41}_{14}$Si$_{27}$ to study how collectivity impacts the low-lying structure of $N = 27$ neutron-rich nuclei.

DOI: 10.1103/PhysRevC.78.034307 PACS number(s): 21.10.Jx, 21.60.Cs, 25.60.−t, 27.40.+z

I. INTRODUCTION

The $N = 28$ shell closure has been extensively studied in the last decade via β-decay measurements [1], Coulomb excitation [2,3], γ- or electron-decay spectroscopy [4–11], mass measurements [12,13], and direct reactions [14,15]. In parallel, numerous theoretical efforts have been carried out both in mean field [16–19] and shell model frameworks [20–24]. These studies have pointed out that the $Z \leqslant 16$ nuclei exhibit collective properties. This feature was ascribed to the erosion of the $N = 28$ shell closure when only four protons are removed from the doubly magic ^{48}Ca. The $_{18}$Ar$_{N\simeq 28}$ nuclei are therefore turning points to understanding the departure from spherical nuclei with single-particle states to deformed nuclei. Previous experimental studies on ^{45}Ar$_{27}$ were carried out by means of one-neutron knockout, β decay of ^{45}Cl, and in-beam γ-ray spectroscopy using the fragmentation reaction. The two first experimental techniques were used to probe the neutron occupied orbitals from which neutrons were either knocked out or converted into a proton by the weak interaction process. The latter experiment favors the production of yrast states and is globally not very selective, thus making the assignment of the excited states difficult. The transfer (d, p) reaction is a suitable tool for determining the single-particle nature of the *valence* neutron states, as shown for $^{47}_{18}$Ar$_{29}$ in Ref. [15]. This method is therefore perfectly adapted to the searching for the evolution of the $N = 28$ shell closure. In the present article, we report on the structure of $^{45}_{18}$Ar$_{27}$ using the same experimental technique as in Ref. [15].

Section II presents a detailed description of the experimental and analysis methods. In Sec. III, results of the distorted-wave Born approximation (DWBA) analysis of the measured proton differential angular distributions are given. The reported structure of ^{45}Ar is interpreted in the shell model framework in Sec. IV, and the discussion is extended to more exotic $N = 27$ isotones, to study if and how collectivity, observed at $N = 28$, impacts the structure of these nuclei.

II. EXPERIMENTAL METHOD

The experiment was performed at the GANIL/SPIRAL facility [25]. The ^{44}Ar nuclei were produced by means of the fragmentation of a 66A MeV ^{48}Ca primary beam into a thick carbon target. The Ar nuclei were extracted from the target heated at a temperature of 2000 K and were purified and accelerated to an energy of 10A MeV by the CIME cyclotron. For checking and calibration purposes, a stable beam of ^{40}Ar was accelerated to an energy of 11A MeV in a dedicated setting. The pure argon beams (10^5 pps on average for both settings) impinged on a 0.38(6) mg cm^{-2} thick CD_2 target. The angular divergence of the beam was set to a low value of 1.5 mrad, as a consequence the full width at half maximum (FWHM) of the beam spot on target was about 1.5 cm along both the x and y axis. One multiwire proportional chamber (MWPC) CATS ("chambre à trajectoire de Saclay" or Saclay trajectory chamber) [26] was placed 11 cm downstream from the target to determine the (x, y) position of the reaction on target, on an event-by-event basis. To achieve this goal, the position on CATS was simply translated on the target along the beam axis direction to deduce the vertex localization. The position resolution of the detector was determined in a

 ©2008 The American Physical Society

dedicated run using a mask with calibrated holes located at the target position. Within the experimental conditions, the image of the mask was reconstructed with a resolution of about 1 mm. The MWPC also served to monitor the beam intensity. The efficiency of the MWPC has been determined relative to a plastic scintillator (assumed to be 100% efficient within the experimental conditions) located behind the CATS detector. The deduced efficiency is 95(5)%.

The outgoing proton in the (d, p) reaction was detected at backward angles in the laboratory frame in one of the eight modules of the double-sided silicon strip detector (DSSD) MUST [27]. The array was arranged in two rings of four modules each, located 10 cm upstream from the target. The internal ring was centered at 110° in the laboratory frame, and the external one at 145°. The total angular coverage ranged from 95° to 175°, in the laboratory frame ($5° < \theta_{\text{c.m.}} < 50°$, where c.m. stands for center of mass). The three-dimensional localization of the detectors was measured with an accuracy of 0.5 mm by means of a laser positioning device.

The geometrical efficiency of the array has been simulated taking into account the measured position of each of the modules with respect to the center of the target. The efficiency curve has a double-humped structure (one for each ring) with a maximum efficiency at about 150°, as shown by the set of black points in Fig. 1(a). Uncertainties are less than 10%; these values were determined by shifting the position of the modules by ±0.5 mm in the simulation. Each module has an active area of 60×60 mm^2, divided into 60×60 perpendicular strips (x and y). The angles of emission of the protons were obtained, with a resolution of 1° in the laboratory frame, from the combination of positions at the target and the MUST array.

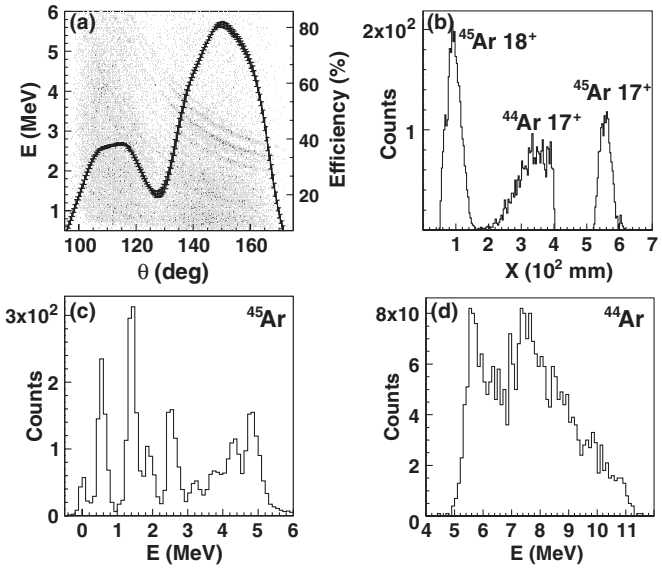

FIG. 1. (a) Kinematic lines of the protons emitted in the ^{44}Ar$(d, p)^{45}$Ar reaction together with geometrical efficiency of the charged particle array (black points). (b) Position distribution of the reaction residues at the focal plane of SPEG. (c) Exclusive ^{45}Ar excitation energy spectrum, gated on ^{45}Ar. (d) Same as (c), but gated on ^{44}Ar (see text).

Figure 1(a) also displays the scatter-plot of proton energy versus laboratory angle measured for the ^{44}Ar$(d, p)^{45}$Ar reaction. Kinematic lines are visible corresponding to different final states in ^{45}Ar. The weaker statistics in the angular domain around 130° are due to the low efficiency in this region corresponding to the gap between the external and internal rings. Excitation energies in ^{45}Ar and scattering angles in the center-of-mass frame have been reconstructed using two-body kinematics. To reduce the background, the transfer-like residues were selected and identified by the GANIL energy-loss spectrometer (SPEG) [28]. The detection system at the focal plane consisted of (i) two cathode readout drift chambers (CRDCs) used for a precise determination of the magnetic rigidity of the transmitted nuclei, (ii) an ionization chamber (IC) for energy-loss measurement, and (iii) a plastic scintillator for the measurement of the time of flight with respect to the CATS detector and for the determination of the fragment residual energy. To minimize pileup in both the CRDC and IC, the elastically scattered nuclei were stopped in a movable active "finger" of 120 mm width, placed in front of the detection system.

After traversing the target and CATS detector, the Ar nuclei, initially in the 9^+ charge state, were spread over the three charge states 18^+, 17^+, and 16^+, the relative intensities of which have been measured at the SPEG focal plane to be 50%, 40%, and 10%, respectively. Because of the limited momentum acceptance of the spectrometer (±3.5%), the magnetic rigidity of the spectrometer was set to transmit the two most intense charge states. A typical focal plane position spectrum obtained with the CRDCs is shown for the ^{44}Ar$(d, p)^{45}$Ar reaction in Fig. 1(b). The two peaks at the edges of the focal plane correspond to transmission of ^{45}Ar nuclei in either the 18^+ or 17^+ charge state, as labeled on the figure. The bump centered at 350 mm is due to the detection of ^{44}Ar nuclei originating from the transfer to neutron-unbound states in ^{45}Ar. For these neutron breakup events following the (d, p) transfer, only the 17^+ charge state was transmitted to the focal plane of the spectrometer. The sharp cut in the focal plane positions between $x = 400$ and $x = 520$ mm in Fig. 1 corresponds to the projectile-like particles stopped by the movable finger.

Panels (c) and (d) of Fig. 1 display the ^{45}Ar excitation energy spectra gated on the focal plane position corresponding to transfer toward bound and unbound states, respectively. The neutron separation energy of ^{45}Ar is 5.2 MeV. Figure 2(a) shows the inclusive excitation energy spectrum for ^{45}Ar, reconstructed using only the MUST and CATS detectors. Compared to the exclusive spectra of Figs. 1(c) and 1(d), the inclusive spectrum exhibits background contributions arising from the deuteron breakup and from reactions with the carbon nuclei contained in the CD_2 target that are removed when the coincidence with a transfer-like product in SPEG is imposed. However, a loss of about a factor of 2 in transmission is found, attributed to optical aberrations at the very edges of the focal plane, where the transfer-like nuclei are located. Therefore the exclusive spectrum was used only to ascertain the origin of all the peaks observed in the inclusive data, from which the two estimated background components have been subtracted.

The carbon-induced background was determined in a dedicated run using a pure carbon target. This component,

normalized to the number of C nuclei in the CD_2 target and the number of incident particles, accounts for the negative excitation energy part of the ^{45}Ar spectrum presented in Fig. 2(a). The deuteron breakup induced background was determined through a Monte Carlo phase-space calculation giving the relation between the proton energies and angles [29]. The amplitude of this contribution was normalized to reproduce the high-energy tail of the inclusive spectrum of Fig. 2(a). The corresponding background-subtracted spectrum is presented in Fig. 2(b) for ^{45}Ar. A similar procedure has been applied to the case of ^{41}Ar, leading to the excitation energy spectrum presented on Fig. 2(c).

III. RESULTS

In this section, excitation energies of the states populated in ^{41}Ar and ^{45}Ar are reported, as well as the transferred angular momenta and spectroscopic factors resulting from the DWBA analysis of the proton differential angular cross sections. Details on the uncertainties arising from the analysis procedure are also provided.

A global fit of the spectra displayed in Figs. 2(b) and 2(c) was performed with a sum of Gaussians, taking a common FWHM = 280 keV for each peak. The mean excitation energies resulting from the fit are reported in Table I. Eleven states were identified in ^{45}Ar, seven of which for the first time. Quoted errors on excitation energies include statistical errors, propagated uncertainty on the energy calibration of the DSSDs ($\simeq$30 keV), and the uncertainty on the reconstructed angle of emission of the proton ($\simeq$50 keV). To minimize this last contribution to the total uncertainty, the positions of the DSSDs were constrained using the data obtained on the transfer reaction with the stable ^{40}Ar beam. The two first excited states in ^{45}Ar [5] as well as the Q values for the transfer reaction with both ^{40,44}Ar beams [30] also served this purpose, since they were known prior to this experiment, with good accuracy (about 10 keV for the worst case).

The excitation energy spectra of ^{41,45}Ar were divided into 6° wide slices (in the laboratory frame) to deduce the differential cross sections of the populated states. The uncertainties on these cross sections arise from statistics, background normalization, thickness of the CD_2 reaction target, incident number of particles, and geometrical efficiency.

TABLE I. Excitation energies E^* in keV, angular momenta ℓ, and vacancy values $[J] \cdot C^2S$ deduced from the present experiment for ^{41,45}Ar, compared with previous experimental results. For previous work the spin/parity $[(2J)^\pi]$ is also reported when available. The symbol $[J]$ means $(2J + 1)$.

Previous work			Present work		
E^*	ℓ, $(2J)^\pi$	$[J] \cdot C^2S$	E^*	ℓ	$[J] \cdot C^2S$
		$^{41}Ar_{23}$			
0	3, 7^-	3.12[a], 4.24(72)[b]	0(60)	3	2.96(48)
516(2)	1, 3^-	0.28[a], 0.36(8)[b]	575(60)	1	0.32(8)
1357(2)	1, 3^-	1.48[a], 1.68(32)[b]	1360(60)	1	1.92(36)
2398(3)	1, 1^-	0.26[a], 0.30(6)[b]	2435(70)		
3327(4)	1, 1^-	0.58[a], 0.72(12)[b]	3320(60)	1	0.58(12)
3968(2)	1, 1^-	0.94[a], 0.80(14)[b]	3970(60)	1	0.72(14)
		$^{45}Ar_{27}$			
0[c,d,e]	3, 7^-		0(60)	3	1.52(40)
535(5)[c,d,e]	1, 3^-		550(60)	1	0.76(20)
1415(10)[d,e]			1420(60)	1	1.08(16)
1765(14)[c]	–, $(1, 3)^-$		1880(60)	1	0.32(2)
			2510(60)	1	0.46(6)
			3230(60)		
			3720(85)		
			4280(65)		
			4770(60)	3	1.08(24)
			4770(60)	4	2.10(40)
			5630(115)	3	1.14(18)
			5630(115)	4	2.20(40)
			7290(60)		

[a]Reference [32].
[b]Reference [33].
[c]Reference [5].
[d]Reference [34].
[e]Reference [14].

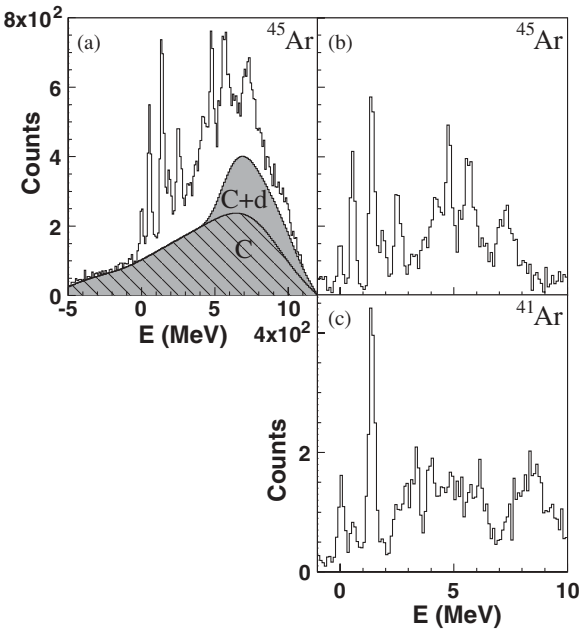

FIG. 2. (a) Inclusive excitation energy spectrum of ^{45}Ar. The dashed grey area (labeled C) corresponds to the measured carbon-induced background. The grey area (C+d) is the sum of the carbon and deuteron breakup-induced backgrounds. Background-subtracted inclusive excitation energy spectra are shown for (b) ^{45}Ar and (c) ^{41}Ar nuclei.

The total uncertainty for each point of the differential cross sections presented in Figs. 3 and 4 is dominated by statistical error. DWBA calculations were performed using the DWUCK4 code [31], assuming $\ell = 1$, 3, and 4 units of transferred angular momenta for each significantly populated state in the neutron transfer reaction. Given the limitations of the present work (beam intensity of about 10^5 pps and 53.5 h beam time), the minimum measurable differential cross section is of the order

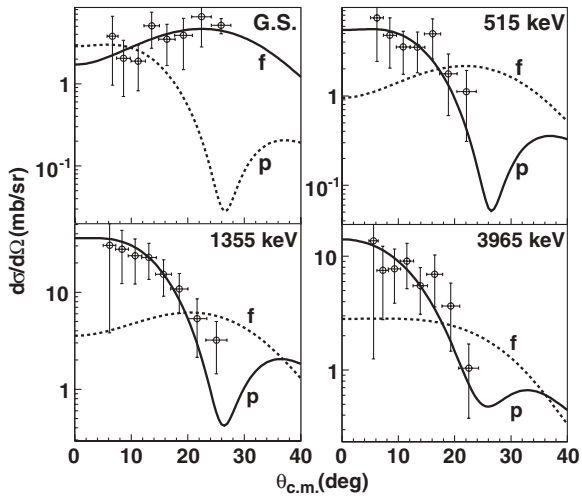

FIG. 3. Proton angular distributions, in the center-of-mass system, of the states populated in ^{41}Ar, labeled by their excitation energies. DWBA curves, for $\ell = 1(p)$ or $\ell = 3(f)$ units of transferred angular momenta, are fitted to the data points.

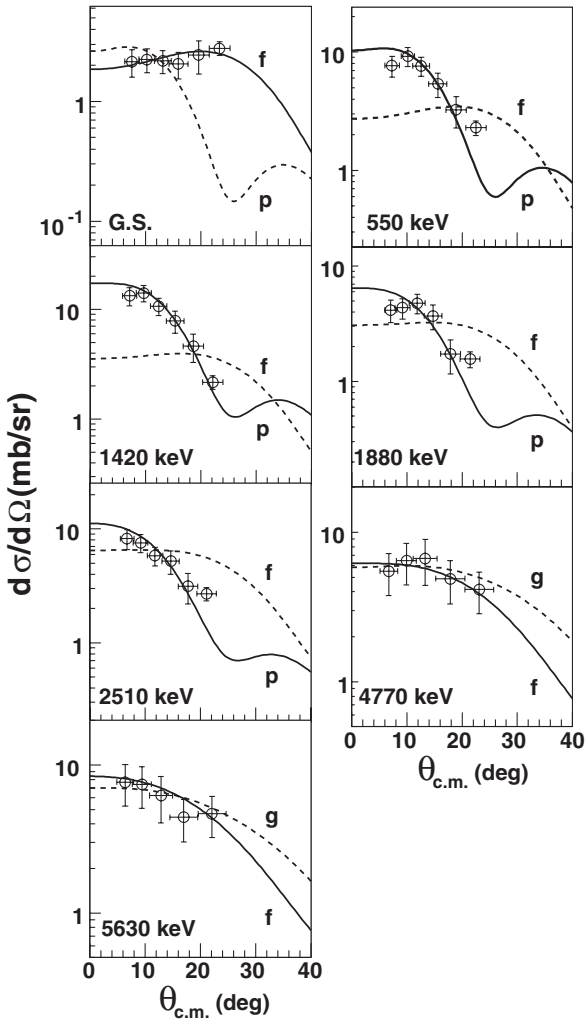

FIG. 4. Same as Fig. 3, but for ^{45}Ar. $\ell = 4$ units of transferred angular momentum (g) is also considered.

of 1 mb sr.$^{-1}$. Global optical potentials, especially suited for the studied mass region and energy of the reactions, were used for both entrance (d+^{40,44}Ar) [35,36] and exit (p+^{41,45}Ar) [37,38] channels. The neutron form factor was calculated using a Woods-Saxon shaped potential, parameters of which were adjusted to reproduce the binding energy and quantum numbers of the populated state. The DWBA predictions were fitted to the experimental data points, allowing one to deduce (i) the transferred angular momentum from the shape of the distribution and (ii) the spectroscopic factors from the relative normalization between the calculation and the data points. Results of the fit are displayed on Figs. 3 and 4; the presented DWBA curves being calculated with the potentials from Refs. [35,37]. Results for ^{41}Ar are compatible with previously reported work, ascertaining the present experimental and analysis procedure. For all significantly populated states, except the ones at 4.7 and 5.6 MeV in ^{45}Ar, the angular momentum is unambiguously attributed. The shapes of the angular distribution corresponding to $\ell = 3$ and 4 units of transferred momentum are too similar to be disentangled for the 4.7 and 5.6 MeV states in ^{45}Ar.

Spectroscopic factors are found to vary within 15%, depending on the set of optical potential used in the DWBA calculations, while the shapes of the distributions are independent of this choice. In Table I, the vacancy values, corresponding to the product of the deduced spectroscopic factors by the spin factor $2J + 1$ (noted as $[J] \cdot C^2S$), are the mean values deduced from adjustments using the four sets of potentials.

IV. DISCUSSION

This section aims at determining how the onset of collectivity impacts the low-lying structure of $N = 27$ isotones from $_{20}$Ca to $_{14}$Si. The known low-lying structure of ^{47}Ca and that reported here for ^{45}Ar will serve as anchors for discussing the structure of S and Si isotones. In the shell model (SM) framework, collectivity is equivalent to the superposition of several particle-hole (p-h) components beyond the assumed close core in the wave functions (WFs) of the states of interest. Therefore an original representation of the WFs of the calculated states in terms of proton (N_π) and neutron (N_ν) p-h configurations will serve to determine the degree of collectivity of the nuclei under consideration.

The experimental data on ^{47}Ca and ^{45}Ar are compared with SM calculations performed with the ANTOINE code [39,40] using a modified version of the $sdfp$ interaction [41]. A detailed discussion of these modifications, leading to the SDPF-NR interaction, is presented in Ref. [42]. The full sd (fp) valence space was considered for proton (neutron) excitations. Using such a valence space for studying the nuclei of interest is valid under the reasonable assumption that the $Z = 20$ and $N = 20$ gaps preclude nucleon excitations from sd to fp orbits. In ^{47}Ca, the sd shell is completely filled. Therefore only the 0p-0h proton configuration exists within this valence space. With respect to a ^{48}Ca core, the ground state configuration of ^{47}Ca is mainly represented by the 0p-1h neutron configuration. It corresponds to a hole in the neutron $\nu f_{7/2}$ orbit, and no particle in the $\nu p_{3/2}$ and upper orbits. For lighter Z nuclei, proton excitations within the sd shells are allowed, together with neutron excitations within the fp shells. Proton excitations of even-Z nuclei follow the general form

$$N_\pi \text{p-}(N_\pi)\text{h}, \quad N_\pi = 0, 1, 2, \ldots .$$

In a similar manner, neutron excitations of odd-N nuclei are expressed as

$$N_\nu \text{p-}(N_\nu + 1)\text{h}, \quad N_\nu = 0, 1, 2, \ldots .$$

These expressions will be used extensively and commented on in the following discussion.

In ^{47}Ca, the measured spectroscopic factors of the ground state and first excited state at 2.02 MeV [43] contain more than 80% of the sum rule limit for the neutron single-particle $f_{7/2}$ and $p_{3/2}$ states, respectively. As stated earlier, the $7/2^-_1$ ground state corresponds to a 0p-1h neutron configuration, where a single hole remains in the $\nu f_{7/2}$ orbit. The $3/2^-_1$ first excited state has an almost pure 1p-2h neutron configuration, with a single neutron promoted into the $\nu p_{3/2}$ orbit and two remaining holes in the $\nu f_{7/2}$ one. In the SM framework, this state is calculated at 2075 keV, in good agreement with experiment. The calculated WFs of the $7/2^-_{gs}$ and $3/2^-_1$ states in ^{47}Ca are presented in the two-dimensional plot displayed in Fig. 5. In this figure, each panel represents the WF of a state in the considered nucleus, as labeled on the figure. The WF of each state is decomposed in terms of its proton (N_π on the y axis) and neutron (N_ν on the x axis) p-h configurations. The percentage of the WF for a couple of (N_π-N_ν) values is proportionnal to the area of the box centered at (N_π-N_ν). Only the percentages larger than 5% have been reported on the figure. For the sake of precision, each percentage is indicated near its corresponding box. As seen from the first row of Fig. 5, the calculated WFs of the $7/2^-_1$ and $3/2^-_1$ states in ^{47}Ca exhibit quasipure configurations with $N_\nu = 0$ (0p-1h) and $N_\nu = 1$ (1p-2h), respectively. We remind the reader that, being restricted to the sd valence space, the only possible proton configuration in ^{47}Ca is $N_\pi = 0$ (0p-0h).

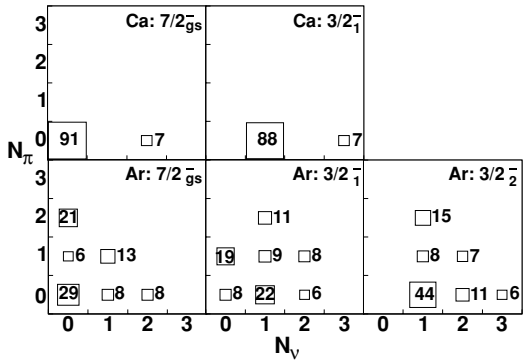

FIG. 5. Squared WF of the first $7/2^-$ and $3/2^-$ states in ^{47}Ca (upper panels) and ^{45}Ar (lower panels) isotones, in the proton (N_π) vs neutron (N_ν) particle-hole configuration plane (see text for details). Excitation energies of the states are given in the text.

Compared with $^{47}_{20}$Ca$_{27}$, the $^{45}_{18}$Ar$_{27}$ nucleus has a more complex low-lying structure, mainly because proton excitations are no longer hindered. Five states have been found in the present experiment below an excitation energy of 2.5 MeV, as shown in Fig. 6. The states discovered in Refs. [5,14], are labeled by a

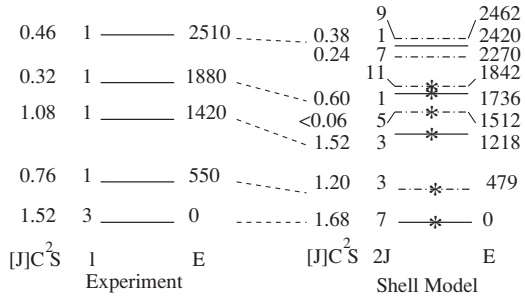

FIG. 6. Experimental level scheme of ^{45}Ar, deduced from the present work, compared with SM calculation. States are labeled by their excitation energies E in keV, orbital angular momentum l, spin ($2J$), and vacancy values $[J] \cdot C^2S$, with $[J] = (2J + 1)$. The calculated levels shown as dashed lines are identified as core excited states (see text). Experimental levels observed in previous works [5,14] are tentatively identified with the shell model levels marked with stars (*).

star (*) in this figure. The agreement between experimental and calculated excitation energies, angular momenta, and spectroscopic factors is satisfactory. Minor discrepancies on spectroscopic factors exist for the states arising from recouplings to core excitation (indicated by dashed lines in the SM level scheme in Fig. 6). Coupled-channels reaction calculations could provide a better description of the measured differential cross sections of these peculiar states. Such a treatment is left for future work. The angular momentum of the ground state is $\ell = 3$, whereas the next four other states have $\ell = 1$. None of the reported spectroscopic factors of these $\ell = 1$ states exhaust the corresponding single-particle strength. This picture contrasts drastically with the one in ^{47}Ca. This comparison already points toward an enhancement of configuration mixing below the $Z = 20$ shell, as described in the following.

The mixing of configurations is clearly seen while looking at the WFs of the first three states of ^{45}Ar, $7/2^-_{gs}$, $3/2^-_1$ and $3/2^-_2$, displayed in the lower panels of Fig. 5. The proton and neutron excitations reported in the figure for ^{45}Ar are built on the following reference configuration: $(\pi d_{5/2})^6$ $(\pi s_{1/2})^2$ $(\pi d_{3/2})^2$-$(\nu f_{7/2})^8$. The WFs of these states span over several neutron and proton configurations in the (N_ν, N_π) particle-hole representation. The neutron configuration of the $7/2^-_{gs}$ is peaked at $N_\nu = 0$ (0p-1h), which corresponds to a neutron $f_{7/2}$ hole configuration. As the proton $\pi s_{1/2}$ and $\pi d_{3/2}$ orbits are quasidegenerate in energy [44], pairing-like excitations are also favored. This explains the equivalent partition of the WF between $N_\pi = 0$ and $N_\pi = 2$ proton configurations. Additionally, 13% of the WF is present at $(N_\nu = 1, N_\pi = 1)$. It corresponds to a configuration where the $\nu p_{3/2}$ unpaired neutron couples to a 2^+ state built on the proton 1p-1h $[(\pi s_{1/2})^1(\pi d_{3/2})^3]$ quadrupole coupling.

As for ^{47}Ca, a $3/2^-$ excited state with an $(N_\nu = 1, N_\pi = 0)$ configuration is expected in ^{45}Ar. From Fig. 5, it is seen that the $3/2^-_2$ state at 1.42 MeV is likely to correspond to the $3/2^-_1$ state at 2 MeV in ^{47}Ca, as their wave functions are peaked at a similar neutron configuration. When summed over the corresponding proton p-h configurations ($N_\pi = 0$, 1, and 2 in Fig. 5), about 70% of the WFs of the $3/2^-_2$ state in ^{45}Ar are exhausted by the $N_\nu = 0$ configuration. This makes the link between this latter state and the $3/2^-_1$ state in ^{47}Ca more apparent.

Conversely, the $3/2^-_1$ state in ^{45}Ar at 550 keV exhibits a complex superposition of various values of N_π and N_ν ranging from 0 to 2. For this state, however, one can distinguish equal contributions (about 20% as seen on Fig. 5) of $(N_\nu = 1, N_\pi = 0)$ and $(N_\nu = 0, N_\pi = 1)$ configurations. The former configuration resembles that of the $3/2^-_2$ state, whereas the second is due to the coupling of a $\nu f_{7/2}$ hole with the 2^+ built on proton excitations. This $3/2^-_1$ state has no counterpart in the low-energy spectrum of ^{47}Ca, as proton excitations are weakened there. The strong configuration mixing found in the present SM calculations accounts for the low excitation energy of this $3/2^-$ state in ^{45}Ar.

Other components of the multiplet originating from the $\nu f_{7/2} \otimes 2^+$ recoupling ($J = 5/2, 7/2, 9/2, 11/2$) have a negligible single-particle character, contrary to the $3/2^-_1$ state. Therefore, these states (indicated with dashed lines in Fig. 6)

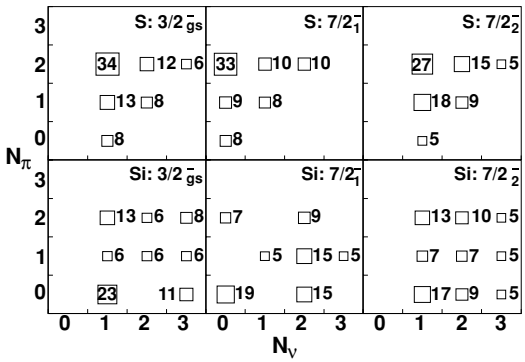

FIG. 7. Same as Fig. 5, but for ^{43}S and ^{41}Si nuclei.

are not populated by the stripping (d, p) reaction. Rather good candidates for the $5/2^-$ and $11/2^-$ states of the multiplet are reported in Ref. [5] using in-beam γ spectroscopy following projectile fragmentation. The predicted $\ell = 1$, $J^\pi = 1/2^-$ states are also seen in the present experimental spectrum, at 1.88 and 2.51 MeV. Their WFs show a mixing of the $\nu p_{1/2}$ single-particle component (about 20% of the WFs) and the $\nu p_{3/2} \otimes 2^+$ recoupling (about 50% of the WFs). This explains why their spectroscopic factors are not close to unity, as it should be for unmixed states.

Shell model calculations have been undertaken for the ^{43}S and ^{41}Si nuclei as well. The WFs for the first $3/2^-_1$ and $7/2^-_{1,2}$ states are shown in Fig. 7. For ^{43}S, the reference configuration on which the p-h configurations, reported in Fig. 7, are built is $(\pi d_{5/2})^6(\pi s_{1/2})^2$-$(\nu f_{7/2})^8$. For ^{41}Si, the reference configuration is $(\pi d_{5/2})^6$-$(\nu f_{7/2})^8$. In SM calculations, the excitation energies of the states shown in Fig. 7 for ^{43}S are $E(7/2^-_1) = 700$ and $E(7/2^-_2) = 950$ keV. These values have to be compared with the experimental ones: $E(7/2^-_1) = 319(2)$ keV [12] and $E(7/2^-_2) \simeq 940$ keV [3]. No experimental data are available for ^{41}Si. The states shown in Fig. 7 for this nucleus are calculated at $E(7/2^-_1) = 140$ and $E(7/2^-_2) = 875$ keV.

At first glance, it is seen that the configuration mixing is growing farther in the lighter $N = 27$ isotones. Even if highly mixed in both cases, the structures of the S and Si isotones differ noticeably. In the ^{43}S nucleus, proton excitations within the $s_{1/2}$-$d_{3/2}$ doublet of orbits easily develop, as indicated by the peaked WF at $N_\pi = 2$. Conversely, proton excitations are more hindered in ^{41}Si, as they require to cross the $Z = 14$ shell gap. As discussed in Ref. [45], proton excitations are weaker in the Si than the S chain but must be present to account for the low 2^+ energy of ^{42}Si [11]. All states shown in ^{41}Si exhibit a larger range of neutron configuration than in the heavier isotones. This has been ascribed to the global shrink in energy of all neutron fp orbits between $Z = 20$ and $Z = 14$ [11].

Noteworthy is the inversion between the natural neutron 0p-1h ($N_\nu = 0$) and the 1p-2h ($N_\nu = 1$) configurations that is occurring below ^{45}Ar. The $3/2^-_1$-like state in ^{45}Ar is becoming the ground state in ^{43}S and ^{41}Si. For ^{43}S, Sarazin *et al.* [12] evidenced the existence of an isomeric state at 319(2) keV, the decay of which was already interpreted as a $7/2^-_1$ to the $3/2^-_1$ ground state transition. To obtain a deeper understanding of the origin of this inversion, monopole- and multipole-energy

contributions to the total energies of the states of interest have been extracted. The monopole energy represents the mean field contribution, of spherical Hartree-Fock type, to the total energy of the state. As demonstrated in Ref. [46], multipole energy corresponds to correlation contributions. The $7/2^-_1$ state is calculated as the ground state of each studied $N = 27$ isotone at the *monopole* level. The *multipole* energy is found to be about 2, 9, 12, and 15 MeV in Ca, Ar, S, and Si isotones, respectively. This increase of correlation energy along $N = 27$ favors configuration mixing, as shown in Figs. 5 and 7. The energy decomposition also shows that the $3/2^-_1$ states in ^{43}S and ^{41}Si are energetically lowered by about 2 MeV, with respect to the $7/2^-_1$ state, because of a multipole energy gain in the former state. It thus appears that the increase of correlation energies is mainly responsible for the evolution of the low-lying structure along $N = 27$. Similar results on the role of correlations at the $N = 28$ shell closure can be found in Ref. [23], in which the authors used an older version of the $sdpf$ interaction [41].

V. SUMMARY

The spectroscopy of ^{45}Ar has been studied through the $d(^{44}\mathrm{Ar}, p)^{45}\mathrm{Ar}$ transfer reaction performed at $10A$ MeV. Excitation energies of 11 states, up to 7.3 MeV, have been reported, 7 of which for the first time. Orbital angular momenta and spectroscopic factors of the most strongly populated states have been deduced from DWBA analysis of the measured proton angular distributions. Below 4.5 MeV, the deduced angular momenta agree with neutron excitations restricted to the fp shell. At higher excitation energies, measured angular distributions are compatible with $\ell = 4$ units of transferred angular momentum. The present data have been successfully interpreted in the shell model framework, using a new $sdpf$ interaction. Core excitations are found to significantly fragment the spectroscopic strength for the low-lying states in ^{45}Ar. The theoretical study has been extended to other $N = 27$ isotones ranging from Ca to Si. Erosion of the $N = 28$ spherical gap and increase of correlation energies have been shown to account for the development of configuration mixing while going away from the β-stability line. The 1p-2h neutron component is found to be the ground state in both ^{43}S and ^{41}Si instead of the natural 0p-1h configuration because of the gain of correlation energy in the former configuration.

ACKNOWLEDGMENTS

L. G. thanks J. P. Delaroche, S. Péru, and J. F. Berger for fruitful and enlightening discussions. K.-L. K acknowledges financial support from Helmholtz Gemeinschaft under Grant VH-VI-061 and from Deutsche Forschungsgemeinschaft (DFG) under Contract KR 806/13-1. K. W. K. was supported by the U.S. National Science Foundation and the State of Florida.

[1] O. Sorlin *et al.*, Phys. Rev. C **47**, 2941 (1993).
[2] H. Scheit *et al.*, Phys. Rev. Lett. **77**, 3967 (1996).
[3] R. W. Ibbotson, T. Glasmacher, P. F. Mantica, and H. Scheit, Phys. Rev. C **59**, 642 (1999).
[4] D. Sohler *et al.*, Phys. Rev. C **66**, 054302 (2002).
[5] Zs. Dombrádi *et al.*, Nucl. Phys. **A727**, 195 (2003).
[6] O. Sorlin *et al.*, Eur. Phys. J. A **22**, 173 (2004).
[7] A. Gade *et al.*, Phys. Rev. C **74**, 034322 (2006).
[8] J. Fridmann *et al.*, Phys. Rev. C **74**, 034313 (2006).
[9] S. Grévy *et al.*, Phys. Lett. **B594**, 252 (2004).
[10] S. Grévy *et al.*, Eur. Phys. J. A **25**, s01 111 (2005).
[11] B. Bastin *et al.*, Phys. Rev. Lett. **99**, 022503 (2007).
[12] F. Sarazin *et al.*, Phys. Rev. Lett. **84**, 5062 (2000).
[13] B. Jurado *et al.*, Phys. Lett. **B649**, 43 (2007).
[14] A. Gade *et al.*, Phys. Rev. C **71**, 051301(R) (2005).
[15] L. Gaudefroy *et al.*, Phys. Rev. Lett. **97**, 092501 (2006).
[16] T. R. Werner *et al.*, Nucl. Phys. **A597**, 327 (1996).
[17] G. A. Lalazissis, D. Vretenar, P. Ring, M. Stoitsov, and L. M. Robledo, Phys. Rev. C **60**, 014310 (1999).
[18] S. Péru, M. Girod, and J. F. Berger, Eur. Phys. J. A **9**, 35 (2000).
[19] R. Rodríguez-Guzmán, J. L. Egido, and L. M. Robledo, Phys. Rev. C **65**, 024304 (2002).
[20] J. Retamosa, E. Caurier, F. Nowacki, and A. Poves, Phys. Rev. C **55**, 1266 (1997).
[21] D. J. Dean, M. T. Ressell, M. Hjorth-Jensen, S. E. Koonin, K. Langanke, and A. P. Zuker, Phys. Rev. C **59**, 2474 (1999).
[22] E. Caurier, F. Nowacki, and A. Poves, Eur. Phys. J. A **15**, 145 (2002).
[23] E. Caurier, F. Nowacki, and A. Poves, Nucl. Phys. **A742**, 14 (2004).
[24] E. Caurier, G. Martínez-Pinedo, F. Nowacki, A. Poves, and A. P. Zuker, Rev. Mod. Phys. **77**, 427 (2005).
[25] A. C. C. Villari *et al.*, Nucl. Instrum. Methods B **204**, 173 (2003).
[26] S. Ottini-Hustache *et al.*, Nucl. Instrum. Methods A **431**, 476 (1999).
[27] Y. Blumenfeld *et al.*, Nucl. Instrum. Methods A **421**, 471 (1999).
[28] L. Bianchi *et al.*, Nucl. Instrum. Methods A **276**, 509 (1989).
[29] P. Nyborg and O. Skjeggestad, *Notes on Phase Space in Kinematics and Multiparticle Systems* (Gordon and Breach, New York, 1968).
[30] G. Audi *et al.*, Nucl. Phys. **A729**, 337 (2003).
[31] P. D. Kunz, University of Colorado (unpublished).
[32] W. Fitz, R. Jahr, and R. Santo, Nucl. Phys. **A114**, 392 (1968).
[33] S. Sen *et al.*, Nucl. Phys. **A250**, 45 (1975).
[34] J. Mrazek *et al.*, Nucl. Phys. **A734**, E65 (2004).
[35] W. W. Daehnick, J. D. Childs, and Z. Vrcelj, Phys. Rev. C **21**, 2253 (1980).
[36] G. L. Wales and R. C. Johnson, Nucl. Phys. **A274**, 168 (1976).
[37] R. L. Varner *et al.*, Phys. Rep. **201**, 57 (1991).
[38] G. M. Perey and F. G. Perey, At. Data Nucl. Data Tables **17**, 1 (1976).
[39] E. Caurier, ANTOINE code, IReS, Strasbourg 1989–2002.
[40] E. Caurier and F. Nowacki, Acta Phys. Pol. B **30**, 705 (1999).
[41] S. Nummela *et al.*, Phys. Rev. C **63**, 044316 (2001).
[42] F. Nowacki and A. Poves, arXiv:0712.2936v1[nucl-th].
[43] J. H. Bjerregaard, O. Hansen, and G. Sidenius, Phys. Rev. **138**, B 1097 (1965).
[44] P. D. Cottle and K. W. Kemper, Phys. Rev. C **58**, 3761 (1998).
[45] C. M. Campbell *et al.*, Phys. Lett. **B652**, 169 (2007).
[46] M. Dufour and A. P. Zuker, Phys. Rev. C **54**, 1641 (1996).